Journal of Materials Chemistry B

ROYAL SOCIETY OF CHEMISTRY

PAPER

View Article Online
View Journal | View Issue

Cite this: J. Mater. Chem. B, 2022, 10, 7650

Degradable silk-based soft actuators with magnetic responsiveness†

Niping Deng,[ab] Jinghang Li,[b] Hao Lyu,[b] Ruochuan Huang,[b] Haoran Liu[b] and Chengchen Guo *[bc]

Received 24th June 2022,
Accepted 1st September 2022

DOI: 10.1039/d2tb01328b

rsc.li/materials-b

Soft actuators with stimuli-responsiveness have great potential in biomedical applications such as drug delivery and minimally invasive surgery. In this study, protein-based soft actuators with magnetic actuation are fabricated using naturally occurring silk proteins and synthesized Fe_3O_4 magnetic nanoparticles (NPs). Briefly, magnetic silk films are first prepared by solution casting of a mixture containing silk proteins, synthesized Fe_3O_4 NPs, and glycerol. The molecular structures of the magnetic silk films are characterized by FTIR spectroscopy, which show that the β-sheet content in the films is about 20%. The mechanical tests show that the magnetic silk films can be stretched to over 200% under wet conditions and Young's modulus is estimated to be 4.89 ± 0.69 MPa, matching the stiffness of soft tissues. Furthermore, the enzymatic degradability, good biocompatibility, and *in vivo* X-ray visibility of the films are demonstrated by the *in vitro* enzymatic degradation test, *in vivo* biocompatibility test, and micro-CT imaging, respectively. Degradable silk-based soft actuators with magnetic responsiveness are successfully prepared by thermal forming or plastic molding of the magnetic silk films. The fabricated soft actuators can be actuated and move with precise locomotive gaits in solutions using a magnet. In addition, the retention of the soft actuators and localized drug delivery in gastrointestinal tracts by attaching a magnet to the abdominal skin are demonstrated using model systems. The degradable silk-based soft actuators provide many opportunities for improving current therapeutic strategies in biomedicine.

1 Introduction

Soft actuators made of stimuli-responsive materials have great potential to improve current therapeutic strategies of drug delivery and minimally invasive surgery since they can access the enclosed space noninvasively in living organisms. For instance, soft actuators can operate inside a human body in surgery or endoscopy to achieve their desired functions.[1–5] The soft and flexible nature of the actuators ensures a gentle interaction with a patient.[4,6,7] An optimal soft actuator for biomedical applications should have good biocompatibility, stimuli-responsive actuation, and desired mechanical properties.[1] From a materials science perspective, the materials used in soft actuators need to be biocompatible with the human body or tissues; however, the extent depends on the specific application. In addition, the materials should have stimuli-responsive properties that fulfill functions. Furthermore, the materials also need to match the mechanical properties of human tissues to a certain degree, particularly for implantable soft actuators. In recent years, many soft actuators have been developed based on various mechanisms such as pneumatic,

[a] School of Materials Science and Engineering, Zhejiang University, Hangzhou 310027, China
[b] School of Engineering, Westlake University, Hangzhou 310024, China. E-mail: guochengchen@westlake.edu.cn
[c] Westlake Laboratory of Life Sciences and Biomedicine, Hangzhou 310024, China

† Electronic supplementary information (ESI) available. See DOI: https://doi.org/10.1039/d2tb01328b

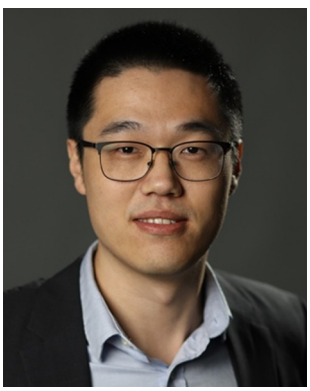

Chengchen Guo

Dr Chengchen Guo is currently an Assistant Professor in the School of Engineering at Westlake University, leading a research team focusing on protein-based functional biomaterials and regenerative medicine. He received his BS degree in Chemistry from Nanjing University and his PhD degree in Chemistry from Arizona State University in 2017. Before joining Westlake University, he was a postdoctoral fellow in the Department of Biomedical Engineering at Tufts University, working with Prof. David L. Kaplan. He has published over 50 peer-reviewed articles with over 1000 citations in high-impact journals, such as Nature Materials, Nature Reviews Materials, and Advanced Functional Materials.

electrostatic, thermal activation, light activation, and magnetic actuation.[2,5,6,8–16] Among all types of soft actuators, magnetic soft actuators have attracted a lot of attention recently and have been demonstrated as promising biomedical devices for minimally invasive surgery, *in vivo* imaging, and drug delivery.[17–23] For instance, magnetically steerable tethered devices with equipped probes and cameras have been used in minimally invasive surgery, such as stereotactic neurosurgical procedures for biopsy or deep brain stimulation,[24,25] endoscopy for lung airway[26] or colon lumen inspections,[27,28] eye surgery for treating retinal diseases or cataracts,[29–31] actuator insertion of cochlear-implants,[32,33] and endovascular navigation.[34–37] However, the most widely used materials in the design and fabrication of these soft actuators include metallic materials (*e.g.*, liquid metals) and synthetic polymers (*e.g.*, polydimethylsiloxane and epoxy resins),[4,5,16,38] leading to potential biocompatibility issues in biomedical applications.

Proteins derived naturally from silkworm cocoons and iron oxide nanoparticles (Fe_3O_4 NPs) are FDA-approved and considered suitable biomaterials for various biomedical applications without causing adverse immune responses.[39–42] A broad spectrum of silk-based materials have been developed in recent years, such as films, sponges, hydrogels, and fibers, extending the applications of silk to biomedical research by taking advantage of the biocompatibility and enzymatic degradability of silk-based materials.[42–47] The mechanical properties of silk-based materials can be tailored to match the mechanical properties of human tissues, offering excellent opportunities for tissue engineering, on-skin electronics, and soft actuators.[12,48–50]

In addition, Fe_3O_4 NPs have been widely used in MRI imaging, drug delivery, and photothermal therapy owing to their excellent biocompatibility.[39,51–57] Silk/Fe_3O_4 NP composites have been developed and used in some biomedical applications such as cancer treatment with magnetic hyperthermia[58–60] and tissue engineering.[61–63] However, little study has been done on soft actuators.

In this study, we report a simple approach for fabricating degradable protein-based soft actuators with magnetic responsiveness using silk proteins and Fe_3O_4 NPs (Fig. 1). Briefly, silk films with Fe_3O_4 NPs were prepared by solution casting of a mixture solution containing silk proteins and Fe_3O_4 NPs. Glycerol was used as a plasticizer to tailor the mechanical properties of the materials. The prepared magnetic silk films showed good flexibility, moldability, and tissue-matching mechanical properties in wet conditions. Furthermore, X-ray visibility, *in vitro* enzymatic degradability, and *in vivo* biocompatibility of the magnetic silk films were investigated and proved. Through thermal forming or thermoplastic molding of magnetic silk films, silk-based soft actuators with various 3D structures were fabricated. Soft actuators could perform precise locomotion using a magnet or under a programmable magnetic field. In addition, the localization of magnetic actuators at a specific position in the gastrointestinal tract with controlled drug release capability was demonstrated using a model system. Overall, protein-based soft actuators composed of silk proteins and Fe_3O_4 NPs offer diverse possibilities for improving the therapeutic strategies of drug delivery and minimally invasive surgery in biomedical applications.

2 Experimental section

2.1 Materials and chemicals

Silkworm cocoons (*Bombyx mori*) were purchased from a local store in Hangzhou, China. Sodium carbonate (Na_2CO_3, 99.5%) and lithium bromide (LiBr, 99%) were purchased from Aladdin Co., Ltd and used as received. Glycerol (99%), iron(III) chloride ($FeCl_3{\cdot}6H_2O$, 99%), trisodium citrate (99%), and sodium acetate (CH_3COONa, 99.9%) were purchased from Macklin, Ltd and used as received. Dialysis tubing was purchased from Solarbio Science & Technology Co., Ltd (Beijing, China). Protease XIV from *Streptomyces griseus*, α-chymotrypsin from bovine pancreas, and collagenase I from clostridium were purchased from Sigma Co., Ltd and used as received. Paraformaldehyde (4%) was purchased from Beijing Dingguo Changsheng Biology Co., Ltd and used as received. Hematoxylin and eosin and Masson's trichrome were purchased from HK Biotechnology and used as received.

2.2 Synthesis of iron oxide nanoparticles (Fe_3O_4 NPs)

For the synthesis of Fe_3O_4 NPs, 3.00 g of $FeCl_3{\cdot}6H_2O$ was dissolved in 100 mL of ethylene glycol at 180 °C, followed by the addition of 0.72 g of trisodium citrate. After the complete dissolution of trisodium citrate, 4.80 g of sodium acetate was added to the above solution. After vigorous stirring for 30 minutes, the as-prepared mixture was slowly poured into a Teflon-lined stainless-steel autoclave reactor (volume of ~200 mL), then heated at 200 °C for 10 hours. After the autoclave cooled down to room temperature, the as-prepared Fe_3O_4 NPs were thoroughly washed with ethanol and deionized water several times to remove the byproducts. The purified Fe_3O_4 NPs were re-dispersed in deionized water for further use.

2.3 Preparation of regenerated silk fibroin solution

The regenerated silk solution was prepared according to the reported protocol.[46] Briefly, 10.0 g of cocoons were cut into small pieces and boiled in 0.02 M sodium carbonate for 30 min to remove the sericin (degumming). Degummed silk fibers were collected and washed with DI water several times, followed by air drying at room temperature. Then 5.0 g of dried degummed silk fibers were dissolved in 20 mL of 9.3 M LiBr at 60 °C for about 4 h. Then the solution was dialyzed in DI water (3500 MWCO, Pierce) to remove the salt. The water was changed after 1 h, 4 h, 8 h, 24 h, 36 h, 48 h, and 60 h. After dialysis, the final solution was purified by centrifugation at 9000 rpm for 20 min at 4 °C twice. The concentration of the purified silk solution was determined to be ~6 wt% (w/v)) and the purified silk solution was stored in a 4 °C freezer for further use.

2.4 Preparation of magnetic silk films

50.0 mL of regenerated silk solution (~6 wt%, w/v), 6.4 mL of Fe_3O_4 NP solution (~200 mg mL^{-1}) and 7.5 mL of glycerol

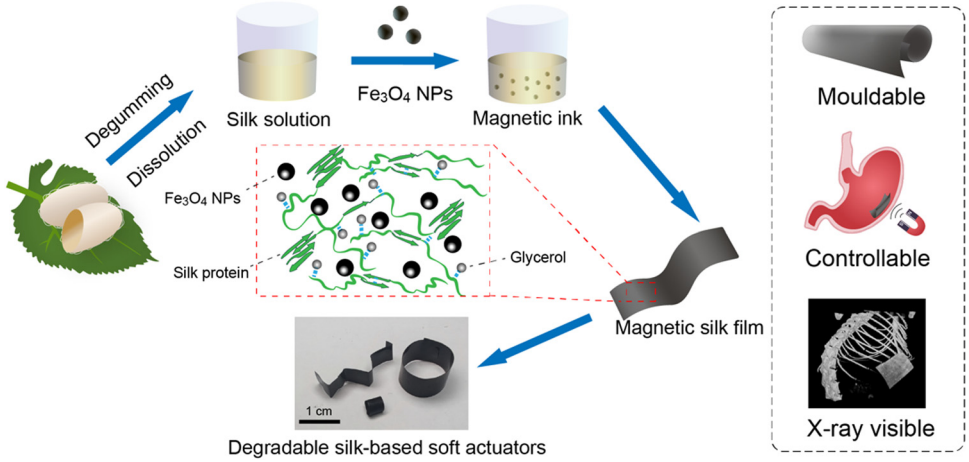

Fig. 1 Schematic illustration of the fabrication of degradable silk-based soft actuators with magnetic actuation.

solution (100 mg mL^{-1}) were mixed to obtain a homogeneous mixture. 3.5 mL of the mixture solution was then poured slowly into a Petri dish with a diameter of 60 mm, followed by drying at 25 °C and 60% relative humidity (RH) overnight to obtain the dried magnetic silk films. The non-magnetic silk films were prepared without incorporating Fe_3O_4 NPs in the system.

2.5 Fabrication of silk-based soft actuators

The silk-based soft actuators were fabricated by thermal forming or plastic molding of the magnetic silk films. When heating up to ~120 °C, the magnetic silk films became soft and could be shaped into various structures, and then they were cooled down to room temperature to obtain silk-based soft actuators with designed structures. In addition, two pieces of the magnetic silk films were thermally welded together by heating up to ~120 °C.

2.6 Scanning electron microscopy (SEM)

The morphologies of the Fe_3O_4 NPs and the magnetic silk films were analyzed using SEM. The SEM images were collected with a voltage of 1.0 kV at different spots for each sample.

2.7 Magnetic testing

The magnetic properties of the Fe_3O_4 NPs and the magnetic silk films were characterized using a Quantum Design MPMS3 SQUID magnetometer. The data were collected at a temperature of 37 °C for all samples.

2.8 Rheology testing

The rheological properties of the silk solutions with or without Fe_3O_4 NPs were characterized on a rheometer (TA-Waters ARES-G2, USA) with a 50 mm plate geometry at 25 °C. The gap between the upper and lower plates was set to 1.2 mm. To ensure the accuracy of the measurement, the gap was filled with the sample with great care to avoid any significant shearing force. Flow sweep was measured to investigate the viscosity of the dope through a logarithmic steady shear rate between 0.01 and 100 s^{-1}.

2.9 Fourier-transform infrared (FTIR) spectroscopy

The FTIR spectra of the prepared Fe_3O_4 NPs and silk films were collected on a Bruker INVENIO S FTIR spectrometer equipped with an attenuated total reflection (ATR) attachment. For each sample, at least three spectra were collected with a resolution of 4 cm^{-1} and 64 scans. A custom-made Python package was used for performing the peak deconvolution of the amide I region. For deconvolution, the Gaussian peaks at 1620 cm^{-1} and 1698 cm^{-1} were attributed to the β-sheet structure, while the Gaussian peaks at 1645 cm^{-1} and 1685 cm^{-1} were attributed to random coil/α-helix and β-turn structures, respectively. The contents of different secondary structures were then estimated from the deconvolution.

2.10 X-Ray diffraction (XRD)

The crystal structures of Fe_3O_4 NPs were characterized by XRD on a Bruker D8 Advance X-ray diffractometer (Bruker, Karlsruhe, Germany). The characterization was performed with a tube voltage of 40 kV, a current of 40 mA, and a plate rotational speed of 15 rad min^{-1}. The X-ray wavelength (λ) was 1.54 Å and the diffraction angle (2θ) was recorded from 5° to 80°.

2.11 Mechanical test

The mechanical properties of the silk films were characterized by tensile testing on a mechanical testing machine (CellScale UniVert, Waterloo, Ontario, Canada). All films were cut into scaled dumbbell-shaped strips according to the ASTM standard D412-A for tensile testing and the thicknesses of the samples were measured prior to testing. For an individual test, a controlled strain rate of 2 mm min^{-1} was applied and the data were collected at a frequency of 15 Hz. For each sample, at least six measurements were tested. For dry samples, the measurements were carried out at room temperature and a RH of 50–60%. For wet samples, the samples were incubated in PBS at 37 °C for 10 min and tested immediately.

2.12 *In vitro* biodegradability test of films

The *in vitro* biodegradability of the silk films was investigated through *in vitro* enzymatic degradation. Protease XIV from

Streptomyces griseus, collagenase I from clostridium and α-chymotrypsin from bovine pancreas were used in this study. The concentrations of protease XIV, α-chymotrypsin, and collagenase I were 5 U mL^{-1}, 80 U mL^{-1}, and 20 U mL^{-1}, respectively. The silk films were cut into small pieces. For each test, about 20 mg of silk film pieces (the exact mass is denoted as m_1) was incubated in 2.0 mL of the specific enzyme solution at 37 °C and a shaking rate of 50 rpm for 0.5, 1, 2, and 3 days. At least three measurements were performed for each condition. The enzyme solutions were replaced every two days. After incubation, the residual solid samples were extracted by centrifugation and cleaned with DI water twice. The residual solid samples were then dried thoroughly in an oven and weighed. The mass is denoted as m_2. The residual mass ratio of the silk films was calculated using the following equation:

$$\text{residual mass ratio} = \frac{m_2}{m_1} \times 100\% \quad (1)$$

2.13 *In vivo* response to silk films

Silk films of 0.5 × 0.5 cm^2 were prepared and implanted subcutaneously into 12 week-old mice (purchased from SLAC-CAS, Shanghai, China) under the protocol approved by Westlake university with #AP-21.043-GCC. Briefly, mice of 30–35 g body weight and either sex were used to carry out the study. The mice were anesthetized at 3% isoflurane before surgery and maintained at 2% during the surgery process. The implanted area was shaved and sterilized using disinfectant and ethanol swabs (3×), and the implanted area was injected subcutaneously with Meloxicam (0.5 mg mL^{-1}) administered at a dose of 1 μL g^{-1} for mitigating pain. The magnetic and non-magnetic silk films were cut into 0.5 × 0.5 cm^2 pieces and sterilized under ultraviolet (UV) radiation exposure for 1 h. The sterilized silk films were then implanted through a 0.5 cm incision in the subcutaneous pocket of the lateral side of the back region and protected using a nonabsorbable nylon suture stitch. There was not any infection at the incision during the healing process based on continuous monitoring and no death was recorded during the entire experimental duration. The animals were sacrificed by cervical dislocation after 1 and 4 weeks for tissue collection. Implanted films were collected along with the surrounding tissue and stained with hematoxylin and eosin (H&E, Sigma-Aldrich, USA) for histological examination. The implanted silk films along with the surrounding tissues were retrieved at predetermined time points (1 week and 4 weeks). After the subcutaneous tissue sections were fixed by 4% paraformaldehyde, hematoxylin and eosin (H & E) staining and Masson's trichrome (MT) staining. Paraffin section staining experiments followed the general protocol recommended by HK Biotechnology. The pictures of subcutaneous tissue sections were taken using a motorized fluorescence microscope (Nikon, Ni-E).

2.14 *In vivo* imaging of the silk film using micro-CT

To verify the feasibility of imaging *in vivo*, micro-CT (Bruker, SkyScan 1276) was used for collecting the images of the magnetic silk film implanted in mice.

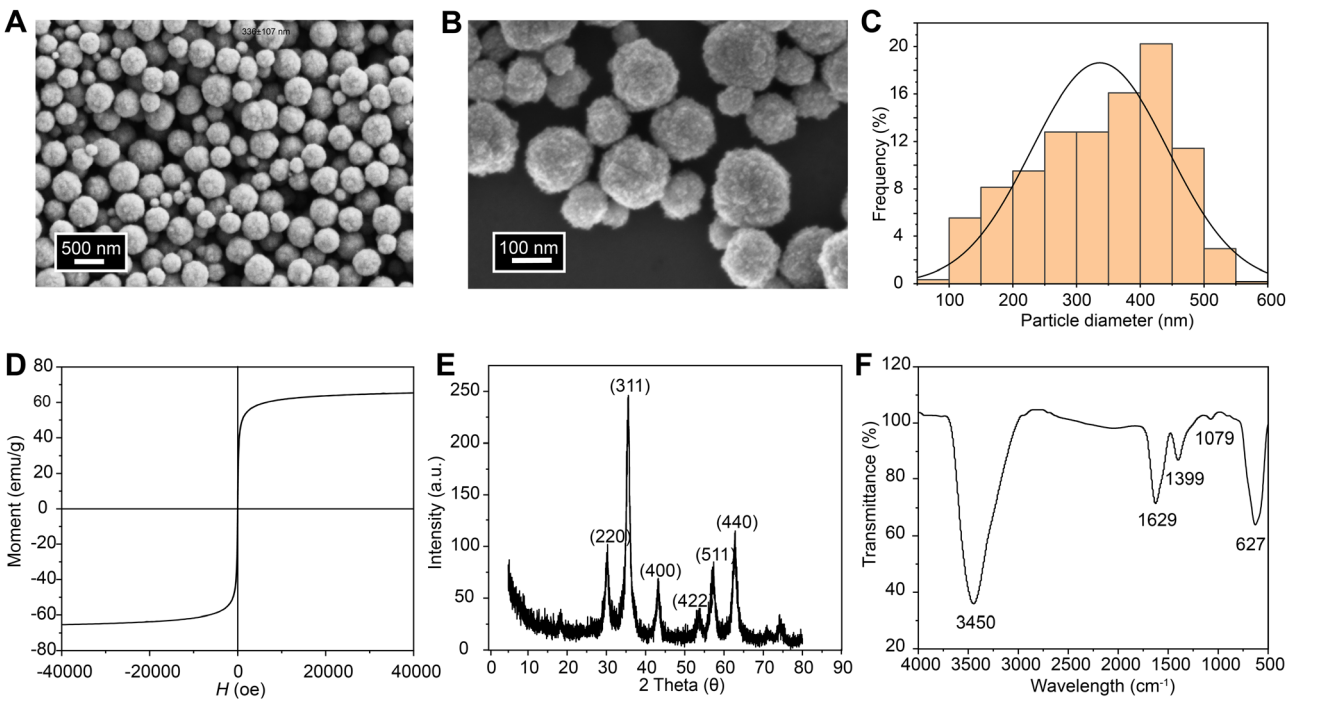

Fig. 2 Characterizations of the synthesized Fe_3O_4 NPs. (A and B) SEM images of the synthesized Fe_3O_4 NPs. (C) Histogram of the particle size distribution. (D) The magnetization curves of Fe_3O_4 particles at 37 °C. Inset: Close-up of the hysteresis at H = 0. (E) The XRD pattern of the synthesized Fe_3O_4 NPs. (F) The FTIR spectrum of the synthesized Fe_3O_4 NPs.

3 Results and discussion

3.1 Characterizations of the magnetic Fe_3O_4 NPs

The morphologies and structures of the synthesized magnetic Fe_3O_4 NPs were investigated by SEM, X-ray diffraction, and FTIR spectroscopy. The obtained magnetic Fe_3O_4 NPs are spherical with rough surfaces and little aggregation (Fig. 2A and B). The particle size distribution was analyzed using ImageJ on multiple images collected at different areas. The diameters of the Fe_3O_4 NPs were mainly in the range of 200–400 nm with an average diameter of 336 ± 107 nm (Fig. 2C). The magnetic properties of the Fe_3O_4 NPs were investigated at a temperature of 37 °C by collecting the magnetization *versus* magnetic field (*M–H*) curve (Fig. 2D). There is no hysteresis in the *M–H* curve of the Fe_3O_4 NPs. The saturation magnetization of the Fe_3O_4 NPs is 65 emu g^{-1}, which is consistent with previously reported work.[64] The XRD pattern of the Fe_3O_4 NPs clearly shows six characteristic peaks (2θ = 30°, 35°, 43°, 53°, 57°, and 62°) that match the profile of pure Fe_3O_4 NPs with a spinal structure (JCPDS file PDF no. 65-3107) (Fig. 2E).[65] The molecular structures of the Fe_3O_4 NPs were characterized by FTIR spectroscopy, and the spectrum is shown in Fig. 2F. The peaks at 3450 cm^{-1} and 1629 cm^{-1} were assigned to the bands of OH stretching and HOH bending, respectively.[66] The peak at 1399 cm^{-1} was assigned to the CO stretching band of primary alcoholic groups at surfaces after washing.[39] The peak at 627 cm^{-1} was assigned to Fe–O stretching.[67,68] Based on the SEM, X-ray diffraction, and FTIR spectroscopy results, the Fe_3O_4 NPs were successfully synthesized for making magnetic silk-based actuators.

3.2 Preparation and characterizations of the magnetic silk films

The magnetic silk films were prepared by solution casting of a mixture of silk proteins, Fe_3O_4 NPs, and glycerol (Fig. 3A). The content of the Fe_3O_4 NPs in the composite is 25% (w/w). Non-magnetic silk films were prepared without the addition of Fe_3O_4 NPs. The rheology test indicated that the addition of the Fe_3O_4 NPs into the silk solution has very little influence on the rheological properties of the mixture solutions (Fig. S1, ESI†). Increasing the content of the Fe_3O_4 NPs in the composite over 40% (w/w) would induce inhomogeneity in the films (Fig. S2, ESI†). The cross-sectional SEM images of the magnetic films showed that Fe_3O_4 NPs dispersed homogenously in the silk matrix without severe particle agglomeration (Fig. 3B and C). The magnetic properties of the magnetic silk film were characterized at a temperature of 37 °C by measuring the magnetization *versus* magnetic field (*M–H*) curve (Fig. 3D). No hysteresis was observed in the *M–H* curves of the magnetic silk film. The saturation magnetization of the magnetic silk film was 22 emu g^{-1}, lower than that of the pure Fe_3O_4 NPs. FTIR spectroscopy was applied to investigate the secondary structures of the silk proteins in the silk films and the spectra are shown in Fig. 3E. The deconvolution of the amide I region (1580–1720 cm^{-1}) was performed to estimate the contents of different secondary structures (Fig. 3F). For the non-magnetic silk films, the β-sheet content was estimated to be ~20%, which is consistent with our previous report.[69] The incorporation of

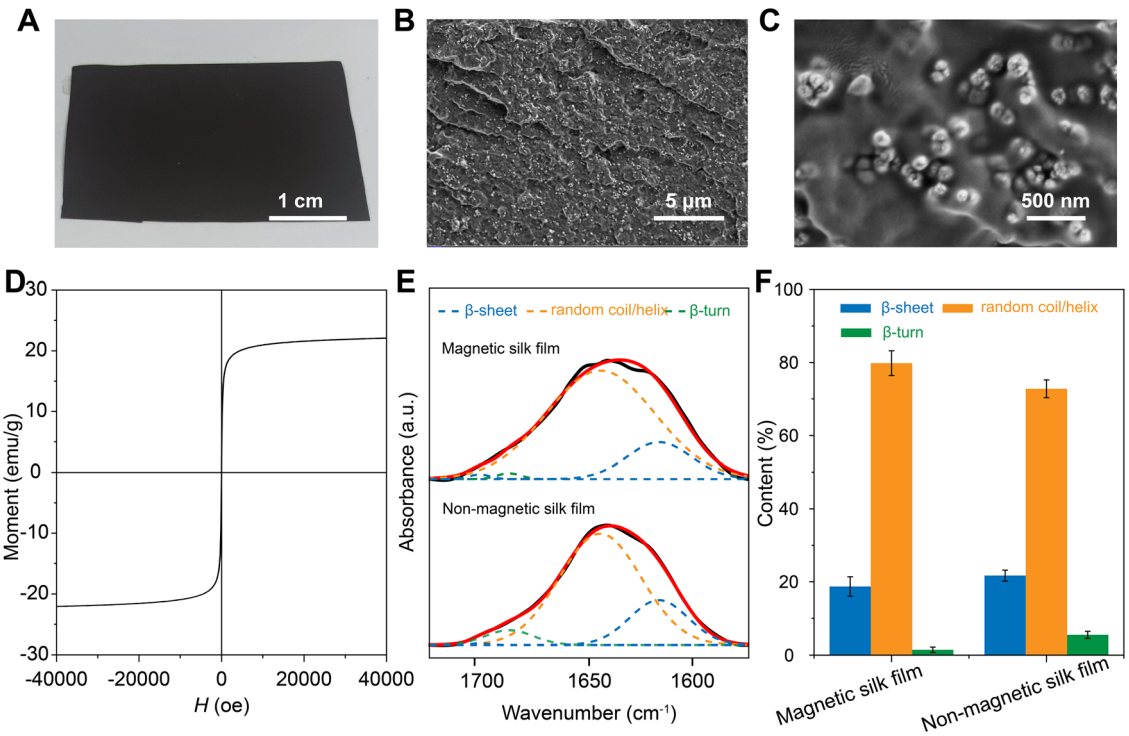

Fig. 3 (A) Photograph of the magnetic silk film. (B and C) SEM images of the magnetic silk film. (D) The magnetization curves of the Fe_3O_4 particles at 37 °C. Inset: Close-up of the hysteresis at H = 0. (E) FTIR spectra of the magnetic and non-magnetic silk films. (F) Secondary structures of the silk proteins in the films from the deconvolution of the amide I region.

the Fe_3O_4 NPs into the films induced a slight decrease of β-sheet content which is likely due to the strong coordination bonding between silk proteins and Fe_3O_4 NPs.[70] In contrast, the contents of random coil/helix and β-turn structures showed slight increases after the introduction of Fe_3O_4 NPs.

3.3 Mechanical properties of the magnetic silk films

The mechanical properties of the magnetic silk films and the non-magnetic silk films were characterized by tensile testing, and the representative stress–strain curves are shown in Fig. 4A. The strain at failure, ultimate strength, Young's modulus, and toughness are summarized in Fig. 4 and Table S1 (ESI†). Under dry conditions, both types of films showed a similar strain at failure of ~150%, an ultimate strength of ~12 MPa, and a toughness of ~20 MJ m^{-3} due to the plasticization by glycerol. The magnetic silk films showed a lower Young's modulus than non-magnetic silk films, which is likely due to the slightly reduced content of β-sheet structure in the magnetic silk films. Under wet conditions, the ultimate strength, Young's modulus, and toughness of both types of films rapidly decreased. However, the strain at failure of the silk films increased. The strains at failure of the magnetic films and non-magnetic films were estimated to be 224 ± 14% and 453 ± 84%, respectively. The Young's modulus of the magnetic silk film was estimated to be 4.89 ± 0.69 MPa, matching the stiffness of the soft tissues (Fig. S3, ESI†).[71] Due to the incorporation of Fe_3O_4 NPs, the magnetic silk films showed a smaller strain at failure (154 ± 24%) but a higher Young's modulus (195.7 ± 53.1 MPa) than the non-magnetic silk films under dry conditions.

3.4 *In vitro* enzymatic degradation of the magnetic silk films

In vitro enzymatic degradation tests were performed to evaluate the degradability of the silk films (Fig. 5). Four solutions were used in this study, including PBS, PBS with 80 U mL^{-1} collagenase I, PBS with 20 U mL^{-1} α-chymotrypsin, and PBS with 5 U mL^{-1} protease XIV. The experiments were conducted at 37 °C with a shaking rate of 50 rpm. When incubated in PBS, the magnetic silk films and non-magnetic silk films showed weight losses of ~15% and ~20%, respectively, which can be attributed to the release of glycerol in the silk films. In PBS with 5 U mL^{-1} protease XIV, both magnetic and non-magnetic silk films showed weight losses of more than 60% and 80%, respectively. Since the Fe_3O_4 NPs cannot be degraded by enzymes,[72] the overall weight loss of the magnetic silk films after enzyme degradation is smaller than that of the non-magnetic silk films. In comparison, the silk films incubated in PBS with 80 U mL^{-1} collagenase I and PBS with 20 U mL^{-1} α-chymotrypsin showed much less weight loss. These results indicated that both magnetic and non-magnetic silk films are enzymatically degradable; however, the silk films have enzymatic

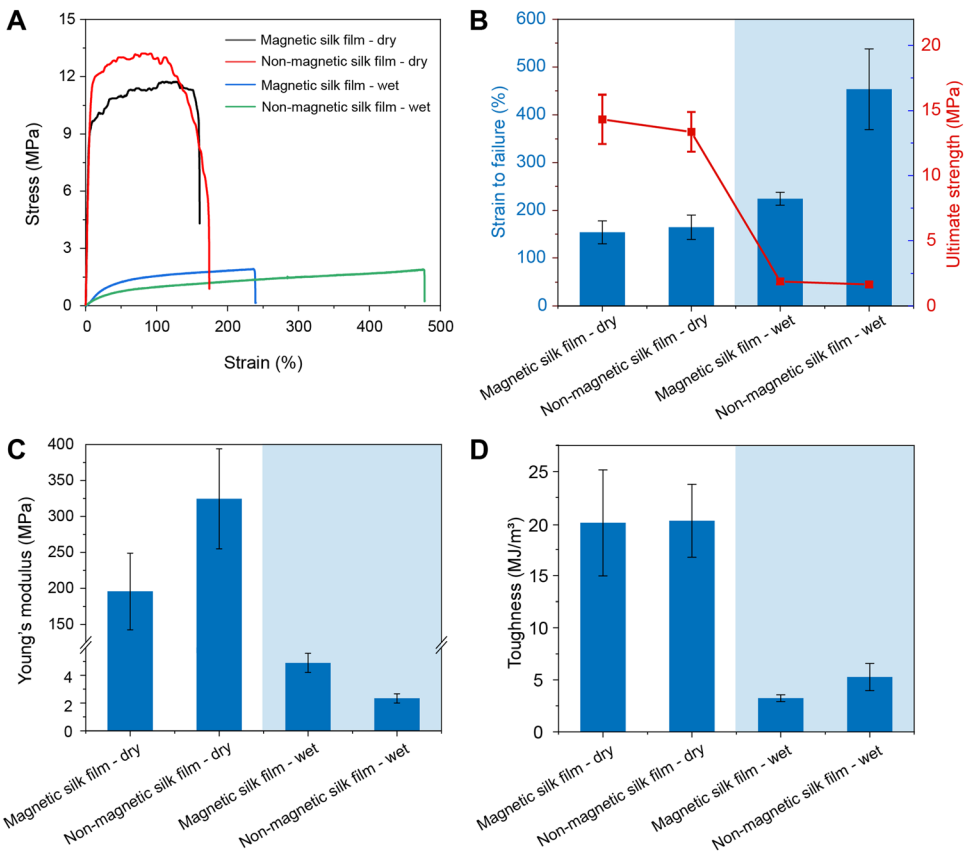

Fig. 4 (A) Representative stress–strain curves of the magnetic and non-magnetic silk films under dry and wet conditions. The summary of strain at failure, ultimate strength (B), Young's modulus (C), and toughness (D) of the magnetic and non-magnetic silk films under dry and wet conditions.

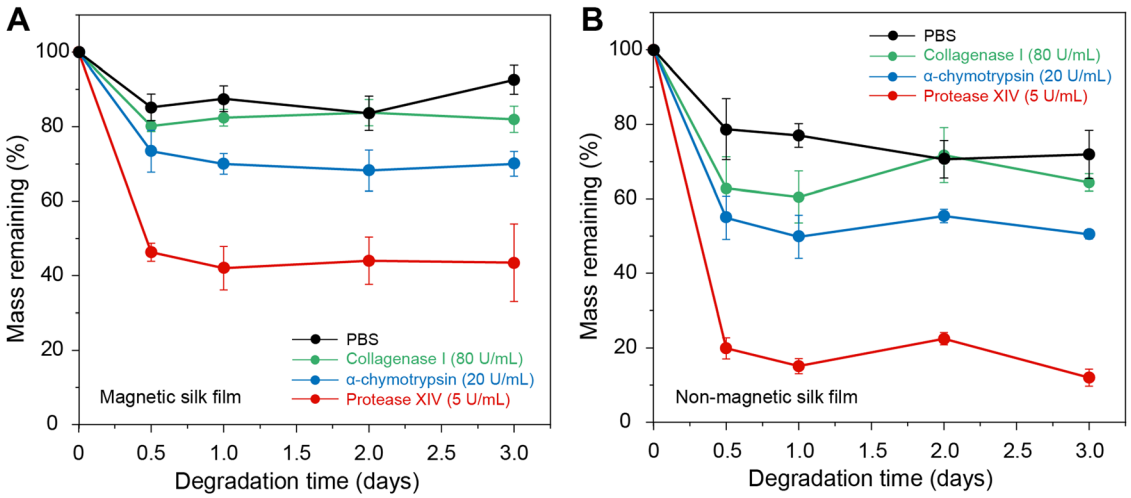

Fig. 5 *In vitro* enzymatic degradation of the magnetic (A) and non-magnetic silk films (B) in different solutions: PBS, PBS with 80 U mL^{-1} collagenase I, PBS with 20 U mL^{-1} α-chymotrypsin, and PBS with 5 U mL^{-1} protease XIV. The experiments were conducted at 37 °C with a shaking rate of 50 rpm.

degradation properties in different enzyme solutions. Furthermore, we characterized the magnetic silk films after *in vitro* enzymatic degradation by SEM and XRD. The SEM results indicated that the morphologies and sizes of the Fe_3O_4 NPs in the films did not change significantly after enzymatic degradation (Fig. S5, ESI†). Moreover, the XRD pattern of the magnetic silk films after enzymatic degradation showed characteristic peaks of the Fe_3O_4 NPs after enzymatic degradation, indicating

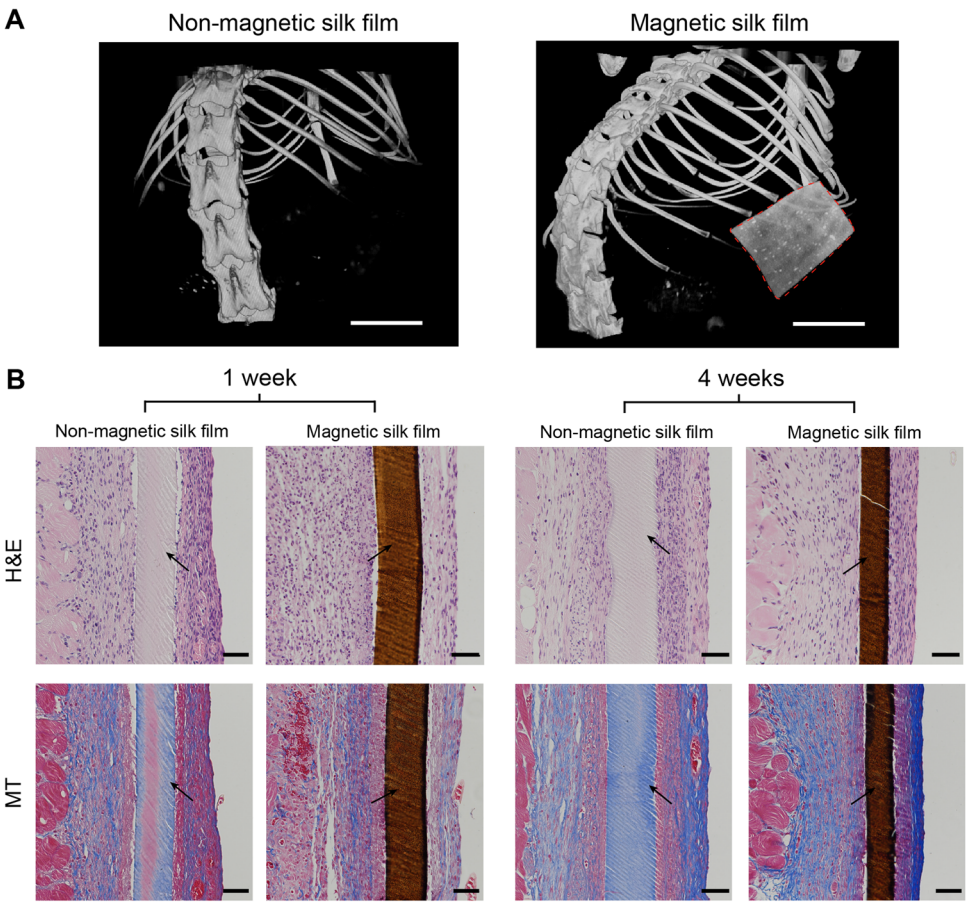

Fig. 6 (A) Micro-CT images of the silk films *in vivo*. The magnetic silk film shown in the micro-CT image is highlighted with red dashed lines. (B) Representative cross-sections of silk films stained with hematoxylin and eosin (H & E) and Masson's trichrome (MT) at 1 week and 4 weeks after implantation. The arrows indicate the implanted films. The scale bars are 5 mm and 50 μm in (A and B), respectively.

that the molecular structures of the Fe_3O_4 NPs did not change significantly (Fig. S5, ESI†).

3.5 *In vivo* responses to the magnetic silk films

To evaluate the *in vivo* biocompatibility of the silk films, the magnetic silk films were subcutaneously implanted in mice and the silk films were retrieved at predetermined time points (1 week and 4 weeks). The magnetic silk films can be imaged by micro-CT scanning *in vivo*, while the non-magnetic silk films were X-ray invisible (Fig. 6A), showing the capability of using micro-CT to track or monitor the magnetic silk-based materials or actuators *in vivo*. One week after implantation, both silk films showed mild inflammatory responses as evidenced by the thin fibrotic capsule, low collagen density, and lack of macrophage infiltration (Fig. 6B). Four weeks after implantation, the collagen density and the thickness of the fibrotic capsules around the materials increased slightly. The similar inflammatory response observed four weeks post implantation indicated that the inflammation persisted for at least four weeks. However, no foreign body giant cells, an indicator of chronic inflammation, were observed at any time point for all implanted silk films. It is concluded that both the magnetic and nonmagnetic silk films showed good biocompatibility.

3.6 Fabrication of silk-based soft actuators with magnetic actuation

Due to the geometrical complexity of psychological tissues and organs, materials with 2D formats, such as films, show a lot of limitations in locomotion and shape change. Here, we have demonstrated the successful transformation of the magnetic silk films to 3D silk-based soft actuators with magnetic actuation by thermal forming or plastic molding.[73,74] When heating up to ~120 °C, the magnetic silk films became soft and could be shaped into various structures, and then they were cooled down to room temperature to obtain silk-based soft actuators (Fig. 7A). The fabricated silk-based soft actuators can be actuated *via* a magnetic field. With a magnet, a silk-based miniature actuator could move under control with precise locomotive gaits inside a narrow tube filled with water (Fig. 7B and Video S1, ESI†). Furthermore, the retention of the soft actuators and localized drug delivery in the gastrointestinal tract by attaching a magnet to the abdominal skin are demonstrated using model systems (Fig. 7C and Video S2 and S3, ESI†). We developed a transparent plastic gastrointestinal model with flowing simulated gastric fluid to mimic the geometry and dimensions of the human stomach. The retention and localization of the miniature soft actuators were investigated based on remote magnetic control. It is found that the magnetic force was able to retain

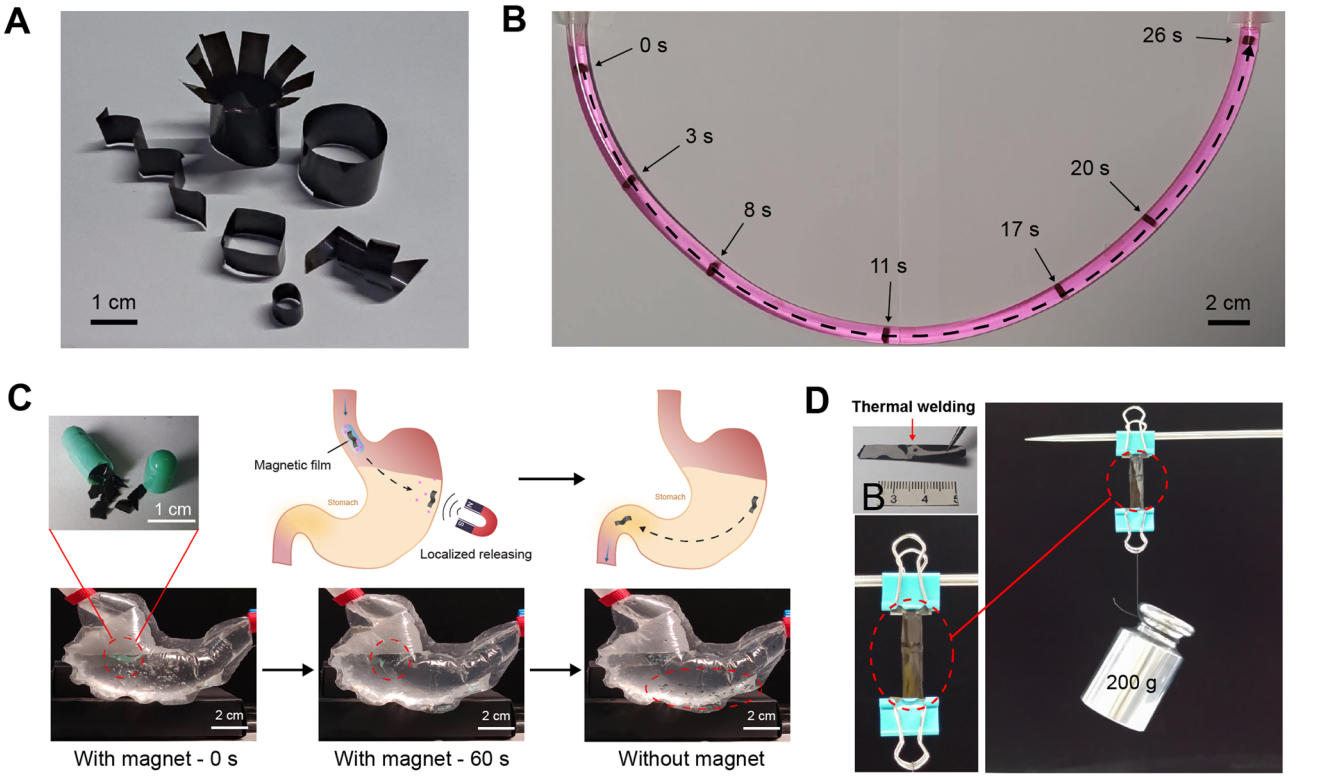

Fig. 7 (A) Fabrication of silk-based soft actuators by thermal forming or plastic molding. (B) Controlled locomotion of a silk-based miniature actuator inside a narrow tube with magnetic actuation. A magnet was placed behind the board to control the actuator. (C) The miniature silk-based soft actuators were encapsulated inside a drug pill to achieve localized drug molecule release at specific sites in the model gastrointestinal tract system with magnetic actuation. (D) Thermal welding of two pieces of the magnetic silk films. The welded film can hold a weight of 200 g.

the miniature soft actuators under fluid flow. When the magnet was removed, the initially retained miniature soft actuators moved forward through the tube (Video S2, ESI†). Encapsulating the miniature actuators into drug pills allows localized drug molecule release at specific sites inside the body with magnetic actuation (Fig. 7C and Video S3, ESI†). Besides the thermal forming of a single magnetic silk film into designed structures, two pieces of the magnetic silk films can be thermally welded together by heating to ~120 °C under a pressure of ~500 kPa. During the welding process, the silk proteins in the films transformed to an intermediate viscoelastic liquid state, leading to the welding of the two silk films.[73,75] The welded film showed good mechanical properties (Fig. 7D). The tensile testing of the welded silk film was carried out in 1× PBS at 37 °C. It is found that the failure or breaking did not occur at the welding position (Video S4, ESI†). The secondary structures of the welded magnetic silk film were investigated by FTIR spectroscopy and no obvious changes in the secondary structures of silk proteins after welding were observed (Fig. S6, ESI†). In summary, a combination of thermal forming and thermal welding provides a convenient way to fabricate various silk-based soft actuators with tailored structures and properties. Due to their good mouldability, excellent biocompatibility, and enzymatic degradability, silk-based soft actuators are expected to provide many opportunities for improving current therapeutic strategies in biomedicine.

4 Conclusions

In this study, we developed protein-based soft actuators using silk proteins and magnetic Fe_3O_4 NPs. The molecular structures, mechanical properties, *in vitro* enzymatic degradability, and *in vivo* biocompatibility of the soft actuators were thoroughly investigated. The results showed that the silk-based soft actuators have an elastic modulus that matches the stiffness of soft tissues, as well as excellent stretchability. Furthermore, *in vitro* enzymatic degradation and *in vivo* biocompatibility tests were carried out to demonstrate the good enzymatic degradability and biocompatibility of the silk-based actuators. The silk-based soft actuators can be actuated and move with precise locomotive gaits *via* a programmable magnetic field. The retention of the soft actuators and localized drug delivery in gastrointestinal tracts by attaching a magnet to the abdominal skin were successfully demonstrated using model systems, showing promising potential in localized drug delivery and minimally invasive surgery in biomedical applications.

Author contributions

Conceptualization, C. G.; methodology, N. D., J. L. and C. G.; software, N. D.; validation, all authors; investigation, N. D. and C. G; data curation, N. D.; writing – original draft preparation, N. D., R. H. and C. G.; writing – review and editing, N. D., R. H. L. and C. G.; supervision, C. G.; project administration, N. D. and C. G.; funding acquisition, C. G. All authors have read and agreed to the published version of the manuscript.

Conflicts of interest

The authors declare no conflicts of interest.

Acknowledgements

This work was supported by the National Natural Science Foundation of China (Grant No. 52103129) and the Foundation of Westlake, Foundation of Westlake Multidisciplinary Research Initiative Center (Grant No. MRIC20210203). The authors thank the Instrumentation and Service Center for Molecular Sciences (ISCMS) and Instrumentation and Service Centers for Physical Science (ISCPS) at Westlake University for the technical support.

References

1 M. Cianchetti, C. Laschi, A. Menciassi and P. Dario, *Nat. Rev. Mater.*, 2018, **3**, 143–153.
2 Z. Zhang, Y. Wang, Q. Wang and L. Shang, *Small*, 2022, 2105116.
3 Y. Kim, G. A. Parada, S. Liu and X. Zhao, *Sci. Robot*, 2019, **4**, DOI: **10.1126/scirobotics.aax7329**.
4 C. S. X. Ng, M. W. M. Tan, C. Xu, Z. Yang, P. S. Lee and G. Z. Lum, *Adv. Mater.*, 2021, **33**, e2003558.
5 W. Hu, G. Z. Lum, M. Mastrangeli and M. Sitti, *Nature*, 2018, **554**, 81–85.
6 X. Liu, Y. Yang, M. E. Inda, S. Lin, J. Wu, Y. Kim, X. Chen, D. Ma, T. K. Lu and X. Zhao, *Adv. Funct. Mater.*, 2021, **31**, 2010918.
7 M. Li, A. Pal, A. Aghakhani, A. Pena-Francesch and M. Sitti, *Nat. Rev. Mater.*, 2022, **7**, 235–249.
8 Q. Li, N. Qi, Y. Peng, Y. Zhang, L. Shi, X. Zhang, Y. Lai, K. Wei, I. S. Kim and K.-Q. Zhang, *RSC Adv.*, 2017, **7**, 17889–17897.
9 G. Manikandan, A. Murali, R. Kumar and D. K. Satapathy, *ACS Appl. Mater. Interfaces*, 2021, **13**, 8880–8888.
10 M. Li, Y. Wang, A. Chen, A. Naidu, B. S. Napier, W. Li, C. L. Rodriguez, S. A. Crooker and F. G. Omenetto, *Proc. Natl. Acad. Sci. U. S. A.*, 2018, **115**, 8119–8124.
11 I. Hwang, H. J. Kim, S. Mun, S. Yun and T. J. Kang, *ACS Appl. Mater. Interfaces*, 2021, **13**, 6597–6605.
12 Y. Wang, W. Huang, Y. Wang, X. Mu, S. Ling, H. Yu, W. Chen, C. Guo, M. C. Watson, Y. Yu, L. D. Black, 3rd, M. Li, F. G. Omenetto, C. Li and D. L. Kaplan, *Proc. Natl. Acad. Sci. U. S. A.*, 2020, **117**, 14602–14608.
13 S. M. Mirvakili and I. W. Hunter, *Adv. Mater.*, 2018, **30**, 1704407.
14 M. Lopez-Valdeolivas, D. Liu, D. J. Broer and C. Sanchez-Somolinos, *Macromol. Rapid Commun.*, 2018, **39**, 1700710.
15 H. Lu, M. Zhang, Y. Yang, Q. Huang, T. Fukuda, Z. Wang and Y. Shen, *Nat. Commun.*, 2018, **9**, 3944.

16 J. Huang, Y. Liu, Y. Yang, Z. Zhou, J. Mao, T. Wu, J. Liu, Q. Cai, C. Peng, Y. Xu, B. Zeng, W. Luo, G. Chen, C. Yuan and L. Dai, *Sci. Robot.*, 2021, **6**, DOI: 10.1126/scirobotics.abe1858.
17 X. Zhao, J. Kim, C. A. Cezar, N. Huebsch, K. Lee, K. H. Bouhadir and D. J. Mooney, *Proc. Natl. Acad. Sci. U. S. A.*, 2010, **108**, 67–72.
18 C. A. Cezar, S. M. Kennedy, M. Mehta, J. C. Weaver, L. Gu, H. Vandenburgh and D. J. Mooney, *Adv. Healthcare Mater.*, 2014, **3**, 1869–1876.
19 S. Yim and M. Sitti, *IEEE Trans. Robot.*, 2012, **28**, 183–194.
20 S. Yim, E. Gultepe, D. H. Gracias and M. Sitti, *IEEE Trans. Biomed. Eng.*, 2014, **61**, 513–521.
21 D. Son, H. Gilbert and M. Sitti, *Soft Robot.*, 2020, **7**, 10–21.
22 S. Kennedy, C. Roco, A. Déléris, P. Spoerri, C. Cezar, J. Weaver, H. Vandenburgh and D. Mooney, *Biomaterials*, 2018, **161**, 179–189.
23 J. Zhang, Z. Ren, W. Hu, H. Soon Ren, C. Yasa Immihan, Z. Liu and M. Sitti, *Sci. Robot.*, 2021, **6**, eabf0112.
24 A. J. Petruska, F. Ruetz, A. Hong, L. Regli, O. Sürücü, A. Zemmar and B. J. Nelson, IEEE International Conference on Robotics and Automation (ICRA), Stockholm, Sweden, May, 2016.
25 A. Hong, A. J. Petruska, A. Zemmar and B. J. Nelson, *IEEE Trans. Biomed. Eng.*, 2021, **68**, 616–627.
26 J. Edelmann, A. J. Petruska and B. J. Nelson, *J. med. robotics res.*, 2017, **03**, 1850002.
27 G. Pittiglio, L. Barducci, J. W. Martin, J. C. Norton, C. A. Avizzano, K. L. Obstein and P. Valdastri, *IEEE Robot. Autom. Lett.*, 2019, **4**, 1224–1231.
28 J. C. Norton, P. R. Slawinski, H. S. Lay, J. W. Martin, B. F. Cox, G. Cummins, M. P. Y. Desmulliez, R. E. Clutton, K. L. Obstein, S. Cochran and P. Valdastri, *Sci. Robot.*, 2019, **4**, DOI: 10.1126/scirobotics.aav7725.
29 S. L. Charreyron, Q. Boehler, A. N. Danun, A. Mesot, M. Becker and B. J. Nelson, *IEEE Trans. Biomed. Eng.*, 2021, **68**, 119–129.
30 S. L. Charreyron, E. Gabbi, Q. Boehler, M. Becker and B. J. Nelson, *IEEE Robot. Autom. Lett.*, 2019, **4**, xvii–xxiii.
31 F. Ullrich, J. Lussi, V. Chatzopoulos, S. Michels, A. J. Petruska and B. J. Nelson, *J. med. robotics res.*, 2017, **03**, 1850001.
32 T. L. Bruns, K. E. Riojas, D. S. Ropella, M. S. Cavilla, A. J. Petruska, M. H. Freeman, R. F. Labadie, J. J. Abbott and R. J. Webster, *IEEE Robot. Autom. Lett.*, 2020, **5**, 2240–2247.
33 L. Leon, F. M. Warren and J. J. Abbott, *J. med. robotics res.*, 2018, **03**, 1850004.
34 A. Azizi, C. C. Tremblay, K. Gagné and S. Martel, *Sci. Robot.*, 2019, **4**, eaax7342.
35 A. Kafash Hoshiar, S. Jeon, K. Kim, S. Lee, J. Y. Kim and H. Choi, *Micromachines*, 2018, **9**, DOI: 10.3390/mi9120617.
36 S. Jeon, A. K. Hoshiar, K. Kim, S. Lee, E. Kim, S. Lee, J. Y. Kim, B. J. Nelson, H. J. Cha, B. J. Yi and H. Choi, *Soft Robot.*, 2019, **6**, 54–68.
37 L. Pancaldi, P. Dirix, A. Fanelli, A. M. Lima, N. Stergiopulos, P. J. Mosimann, D. Ghezzi and M. S. Sakar, *Nat. Commun.*, 2020, **11**, 6356.
38 E. Sachyani Keneth, A. Kamyshny, M. Totaro, L. Beccai and S. Magdassi, *Adv. Mater.*, 2021, **33**, e2003387.
39 B. Chertok, B. A. Moffat, A. E. David, F. Yu, C. Bergemann, B. D. Ross and V. C. Yang, *Biomaterials*, 2008, **29**, 487–496.
40 Y.-L. Su, J.-H. Fang, C.-Y. Liao, C.-T. Lin, Y.-T. Li and S.-H. Hu, *Theranostics*, 2015, **5**, 1233–1248.
41 C. Holland, K. Numata, J. Rnjak-Kovacina and F. P. Seib, *Adv. Healthcare Mater.*, 2019, **8**, e1800465.
42 C. Guo, C. Li, H. V. Vu, P. Hanna, A. Lechtig, Y. Qiu, X. Mu, S. Ling, A. Nazarian, S. J. Lin and D. L. Kaplan, *Nat. Mater.*, 2020, **19**, 102–108.
43 C. Guo, C. Li, X. Mu and D. L. Kaplan, *Appl. Phys. Rev.*, 2020, **7**, 011313.
44 C. Guo, C. Li and D. L. Kaplan, *Biomacromolecules*, 2020, **21**, 1678–1686.
45 C. Li, C. Guo, V. Fitzpatrick, A. Ibrahim, M. J. Zwierstra, P. Hanna, A. Lechtig, A. Nazarian, S. J. Lin and D. L. Kaplan, *Nat. Rev. Mater.*, 2019, **5**, 61–81.
46 D. N. Rockwood, R. C. Preda, T. Yucel, X. Wang, M. L. Lovett and D. L. Kaplan, *Nat. Protoc.*, 2011, **6**, 1612–1631.
47 W. Huang, S. Ling, C. Li, F. G. Omenetto and D. L. Kaplan, *Chem. Soc. Rev.*, 2018, **47**, 6486–6504.
48 R. D. Abbott, E. P. Kimmerling, D. M. Cairns and D. L. Kaplan, *ACS Appl. Mater. Interfaces*, 2016, **8**, 21861–21868.
49 B. Zhu, H. Wang, W. R. Leow, Y. Cai, X. J. Loh, M. Y. Han and X. Chen, *Adv. Mater.*, 2016, **28**, 4250–4265.
50 X. Mu, Y. Wang, C. Guo, Y. Li, S. Ling, W. Huang, P. Cebe, H. H. Hsu, F. De Ferrari, X. Jiang, Q. Xu, A. Balduini, F. G. Omenetto and D. L. Kaplan, *Macromol. Biosci.*, 2020, **20**, e1900191.
51 J. Estelrich, E. Escribano, J. Queralt and M. A. Busquets, *Int. J. Mol. Sci.*, 2015, **16**, 8070–8101.
52 S. M. Dadfar, K. Roemhild, N. I. Drude, S. von Stillfried, R. Knuchel, F. Kiessling and T. Lammers, *Adv. Drug Deliv. Rev.*, 2019, **138**, 302–325.
53 A. Yadav, C. Rao, K. Kaushik, F. Anjum, S. Sharma and C. K. Nandi, *ACS Appl. Nano Mater.*, 2022, **5**, 4018–4027.
54 L. Cera, G. M. Gonzalez, Q. Liu, S. Choi, C. O. Chantre, J. Lee, R. Gabardi, M. C. Choi, K. Shin and K. K. Parker, *Nat. Mater.*, 2021, **20**, 242–249.
55 V. V. Mody, A. V. Singh and B. Wesley, *Appl. Nanosci.*, 2013, **5**, DOI: 10.1515/ejnm-2012-0008.
56 C. Shasha and K. M. Krishnan, *Adv. Mater.*, 2021, **33**, 1904131.
57 K. M. Krishnan, *IEEE Trans. Magn.*, 2010, **46**, 2523–2558.
58 K. Kucharczyk, K. Kaczmarek, A. Jozefczak, M. Slachcinski, A. Mackiewicz and H. Dams-Kozlowska, *Mater. Sci. Eng., C*, 2021, **120**, 111654.
59 H. Zhang, X. Ma, C. Cao, M. Wang and Y. Zhu, *RSC Adv.*, 2014, **4**, 41572–41577.
60 K.-Y. Qian, Y. Song, X. Yan, L. Dong, J. Xue, Y. Xu, B. Wang, B. Cao, Q. Hou, W. Peng, J. Hu, K. Jiang, S. Chen, H. Wang and Y. Lu, *Biomaterials*, 2020, **259**, 120299.
61 C. Zaharia, P. Stanescu, B. Galateanu, M. C. Bunea and E. Vasile, 20th international conference on composite materials, Copenhagen, Denmark, July, 2015.
62 G. F. Yin, Z. B. Huang, M. Deng, J. W. Zeng and J. W. Gu, *J. Colloid Interface Sci.*, 2011, **363**, 393–402.

63 H. Nazari, A. Heirani-Tabasi, M. Hajiabbas, M. S. Bani, M. Nazari, V. P. Mahabadi, I. Rad, M. Kehtari, S. H. A. Tafti and M. Soleimani, *J. Cell. Biochem.*, 2020, **121**, 2981–2993.
64 Y. Ding, Y. Hu, L. Zhang, Y. Chen and X. Jiang, *Biomacromolecules*, 2006, **7**, 1766–1772.
65 G.-Y. Li, Y.-R. Jiang, K.-L. Huang, P. Ding and L.-L. Yao, *Colloids Surf., A*, 2008, **320**, 11–18.
66 M. Omran, T. Fabritius, A. M. Elmahdy, N. A. Abdel-Khalek, M. El-Aref and A. E.-H. Elmanawi, *Appl. Surf. Sci.*, 2015, **345**, 127–140.
67 L. Verdonck, S. Hoste, F. F. Roelandt and G. P. Van Der Kelen, *J. Mol. Struct.*, 1982, **79**, 273–279.
68 M. Gotić and S. Musić, *J. Mol. Struct.*, 2007, **834-836**, 445–453.
69 H. Lyu, Z. Sun, Y. Liu, X. Yu and C. Guo, *Molecules*, 2022, **27**, 1339.
70 Y. Xue, S. Lofland and X. Hu, *Int. J. Mol. Sci.*, 2020, **21**, 7583.
71 A. Miserez, J. C. Weaver and O. Chaudhuri, *J. Mater. Chem. B*, 2015, **3**, 13–24.
72 H. Arami, A. Khandhar, D. Liggitt and K. M. Krishnan, *Chem. Soc. Rev.*, 2015, **44**, 8576–8607.
73 M. A. Brenckle, B. Partlow, H. Tao, M. B. Applegate, A. Reeves, M. Paquette, B. Marelli, D. L. Kaplan and F. G. Omenetto, *Adv. Funct. Mater.*, 2016, **26**, 44–50.
74 M. A. Brenckle, H. Tao, S. Kim, M. Paquette, D. L. Kaplan and F. G. Omenetto, *Adv. Mater.*, 2013, **25**, 2409–2414.
75 M. A. Brenckle, B. Partlow, H. Tao, D. L. Kaplan and F. G. Omenetto, *Biomacromolecules*, 2013, **14**, 2189–2195.

